

Travelling Wave Magnetic Resonance Imaging at 3 Tesla

F. Vazquez, R. Martin, O. Marrufo, and A. O. Rodriguez*

Department of Electrical Engineering, Universidad Autonoma Metropolitana Iztapalapa, Mexico, DF
09340, Mexico

Abstract

Waveguides have been successfully used to generate magnetic resonance images at 7 T with whole-body systems. The bore limits the magnetic resonance signal transmitted because its specific cut-off frequency is greater than the majority of resonant frequencies. This restriction can be overcome by using a parallel-plate waveguide whose cut-off frequency is zero for the transversal electric modes and it can propagate any frequency. To investigate the potential benefits of traveling-wave excitation for whole-body imaging at 3 T, we compare numerical simulations at 1.5 T, 3 T, 7 T, and 9 T via the propagation of the principal mode of a parallel-plate waveguide filled with a cylindrical phantom and two surface coils. B1 mapping was computed and used to investigate the feasibility of the traveling-wave approach at 3T. The point spread function method was used to measure the imager performance for the traveling-wave magnetic resonance imaging experiment. Human leg images were acquired to experimentally validate this approach. The principal mode shows very little variations in the field magnitude along the propagation direction at 3 T when compared to other higher resonant frequencies. The B1 mapping showed that it is possible to conduct experiments using the traveling-wave approach at 128 MHz. The point spread function results showed a good performance of the scanner for these type of experiments. Leg images were obtained with the whole-body birdcage coil and the waveguide with two circular coils for comparison purposes. The simulated and in vivo results correspond very well for both magnetic field and specific absorption rate. A pretty similar performance was observed for the traveling-wave approach and the conventional one. We have demonstrated the feasibility of traveling-wave magnetic for whole-body resonance imaging at 3T, using a parallel-plate waveguide with standard pulse sequences and only one coil array. This extends the use of the waveguide approach to a wider range of resonant frequencies.

*Corresponding author: Alfredo O. Rodriguez, arog@xanum.uam.mx

1 Introduction

The use of travelling waves has been successfully implemented to generate magnetic resonance images (MRI) at 7 T using whole-body systems [1]. This approach allows one to cover samples with larger fields of view using RF coils and a waveguide with different cross-sections. Much work on traveling-wave MRI has been published in the Annual Meetings of the International Society for Magnetic Resonance Imaging in Medicine (ISMRM) and The ISMRM High Field Workshop in Rome since 2008 [2-5]. From these results, it can be observed that the waveguide approach has mainly been tested at 7 T with wide cylindrical bores measuring approximately 60 cm in diameter for human applications. However, other research groups have also investigate the feasibility of this new approach at 9.4T [6]. The aim of this study was to extend this approach to lower magnetic fields than 7 T. To the best of our knowledge, this is the first attempt to use travelling wave MRI at 128 MHz with a 60 cm magnet bore [7]. The cut-off frequency of cylindrical waveguides imposes a limitation on the minimum diameter necessary to transmit a magnetic resonance signal. A 7 T/65 cm MR system is mandatory to transmit MR signals with a circular cross-section waveguide. To overcome this limitation a parallel-plate waveguide (PPWG) was employed because its cut-off frequency is zero for the lowest-order transverse magnetic mode so all frequencies can propagate [8]. Therefore, multinuclear experiments can be performed since a wide spectrum of frequencies can be produced and detected. Simulations of the B1 field were calculated at different resonant frequencies using a simulated cylindrical phantom together with a PPWG with constant cross-section and the results were compared. The Specific Absorption Rate (SAR) was also computed to investigate RF safety. The simulation configurations consisted of one RF coil located at one end of a waveguide to excite an MR signal in the sample, and another one was placed at the opposite end to receive the signal. The distance between these two RF coils is much greater than the actual dimensions of the circular coils. Circular coils were used for reception and transmission of the MR signal in all simulations. There is still some controversy to perform traveling-wave imaging experiments at 3T. A PPWG was built and B1 mapping was carried out to show the feasibility of this approach and, the optimal flip angle for transmission of the RF waves was done too. In addition, the point spread function method was used to estimate the performance of the imager for twMRI. To experimentally test the viability of this approach, images of a healthy volunteer's leg were acquired with the PPWG at 3 T in a clinical MR imager. This imaging experiment was repeated using only a pair of RF surface coils and a whole-body birdcage coil, which is usually embedded in the majority of clinical MR imagers at 3 T and the results were compared.

2 Theory

To understand the propagation of modes in a PPWG, we studied their mathematical description. Full derivations of the electromagnetic equations of PPWG modes may be found in various textbooks [8-9]. Waveguides may be thought of as hollow conductive metal pipes that guide electromagnetic waves. They acts as directors of energy rather than as signal conductors, in the normal sense of the word. The simple waves that a waveguide can transmit are transverse electric (TE) waves of various modes and transverse magnetic (TM) waves. In dealing with transmission inside a hollow conductor, the waveguide consisting of two perfect electrically conducting (PEC) plates is most likely the simplest case. This waveguide offers a straightforward mathematical solution and is commonly found in a number of physics and telecommunications applications. A wave or transverse mode is a particular electromagnetic field pattern of radiation propagated inside a waveguide. Two basic types of transverse modes

can be transmitted and occur because of boundary conditions imposed on the wave by the waveguide. Transverse modes are classified into different types: TE modes (Transverse Electric) and TM (Transverse Magnetic) modes. Maxwell's equations must be solved under particular boundary conditions to calculate the TE and TM modes of a PPWG.

From reference [8], we then have

$$\frac{\partial^2}{\partial z^2} E_y - \frac{\partial^2}{\partial x^2} E_y = \omega^2 \mu \epsilon E_y \quad (1)$$

Eq. (1) describes the transversal electric (TE) modes. Similarly, transversal magnetic TM modes can be derived, such that

$$\frac{\partial^2}{\partial z^2} E_y - \frac{\partial^2}{\partial x^2} E_y = -j\omega\mu \left(\frac{\partial}{\partial z} E_x - \frac{\partial}{\partial x} E_z \right) = \omega^2 \mu \epsilon H_y \quad (2)$$

To determine both the transversal magnetic and electric modes, it is necessary to solve Eqs. (1) and (2).

2.1 Parallel-plate waveguide TE modes

The TE mode has its electric vector in a plane normal to the direction of the propagation, but has a component magnetic field parallel to the direction of propagation. The following boundary conditions were applied: $E_y = 0$ when $x = 0$ and $x = a$, then

$$E_y = j \frac{E_0}{2} (\exp(-j\beta_x x) - \exp(j\beta_x x)) \exp(-j\beta_z z) = E_0 \sin(\beta_x x) \exp(-j\beta_z z) \quad (3)$$

where E_0 is an arbitrary constant. If we assume a perfectly conducting conductor with the boundary conditions above, $\sin(\beta_x a) = 0$, so $\beta_x a = m\pi$, $m = 1, 2, 3 \dots$. Because $m \neq 0$, this implies that the electric field is uniform and tangent to the waveguide plates. The wave constant of propagation is

$$\beta^2 = \beta_x^2 + \beta_z^2 = \omega^2 \mu \epsilon \quad (4)$$

From Eq. (4) the propagation constant along z is

$$\beta_z = \omega^2 - \left(\frac{m\pi}{a} \right)^2 \quad (5)$$

Now, for $\beta \neq 0$ waves can propagate longitudinally in a PPWG, for $\beta > 0$ waves will run parallel along the waveguide plates, and for $\beta < 0$ waves rapidly decay and will not propagate, and the modes are called evanescent modes. Eq. (5) determines the *critical* or *cut-off* frequency, which forms the limit between the transmission and attenuation regions:

$$f_{cut-off} = \frac{m}{2a\sqrt{\mu\epsilon}} \quad (6)$$

for $m = 0, 1, 2, 3 \dots$

2.2 Parallel-plate waveguide TM modes

The transverse magnetic mode is an entirely longitudinal electric field with an axial component of the magnetic field

$$H_y = \frac{H_0}{2} (\exp(-j\beta_x x) - \exp(j\beta_x x)) \exp(-j\beta_z z) = H_0 \cos(\beta_x x) \exp(-j\beta_z z) \quad (7)$$

where H_0 is an arbitrary constant. Assuming the boundary conditions: $x = 0$ and $H_y = H_0$ and, at $x = a$, $\cos(\beta_x a) = 1$ then

$$\beta_x a = m\pi, \quad m = 0, 1, 2, \dots \quad (8)$$

where $m = 0$ implies that a uniform magnetic field tangent to the plates can be formed and is called the Magnetic Transverse (TM) mode. Consequently, the $f_{cut-off}$ (Eq. (6)) becomes zero. The TM_{00} mode is the TEM mode and the dominant mode of the waveguide and it can propagate at any frequency.

3 Numerical simulations

The finite-element method (FEM) is a useful and powerful computational technique for simulating electromagnetic waves that propagate and interact with their surroundings. This method was used due to its ability to model complex geometries with acceptable accuracy. FEM is able to determine propagation characteristics such as loss and dispersion and electromagnetic field distributions as a function of spatial location, frequency, or time. The three-dimensional simulation domain is discretized into tetrahedral mesh elements. To properly simulate wave propagation, the largest mesh element size must be smaller than $\frac{cf_0^{-1}}{3}$ [10], where c is the speed of light and f_0 is the resonant frequency. The experiment was simulated using a time-harmonic solver, such that only one input frequency was considered at a time. The model problem was solved using an iterative generalized minimal residual (GMRES) iterative solver with symmetric successive over relaxation (SSOR) matrix preconditioning [11].

All numerical simulations were performed using COMSOL MULTIPHYSICS (V. 3.2, Comsol, Burlington, MA, USA). The TEM was computed at the following frequencies: 128 MHz, 300 MHz, and 400 MHz (proton resonant frequencies at 3 T, 7 T, and 9 T), along the z -direction using the software above which uses the equations [12]:

$$\nabla \times (\mu_r^{-1} \nabla \times E) - k_0^2 \left(\epsilon_r - j \frac{\sigma}{\omega \epsilon_0} \right) E = 0 \quad (9)$$

$$\nabla \times (n^{-2} \nabla \times H_n) - (\beta_r^2 n^{-2} - k_0^2) H_n = 0 \quad (10)$$

where, $\mu = 4\pi \times 10^{-7} \text{ H/m}$, μ_r is the relative permeability, $\epsilon = \epsilon_0 \epsilon_r$, $\epsilon_r = 1 \times 10^{-9} / 36\pi \text{ F/m}$, ϵ_r is the relative permittivity and ω is the frequency. n represents the refraction index inside the waveguide, the propagation constant is $k_0^2 = k_x^2 + k_y^2 + k_z^2$ and for $k_z = \beta$ represents the propagation constant along the waveguide. To run all simulations, PEC plates were assumed and $p \times E = 0$ (vanishing tangential electric field components at the shield surface).

Two circular surface coils were used for reception and transmission and were located at either end of the waveguide as shown in Fig. 1.a). The surface coils were linearly driven. The waveguide plates were mounted on

an cylinder (diameter = 30 cm, 60 cm long) and assumed to be 25 cm in width.

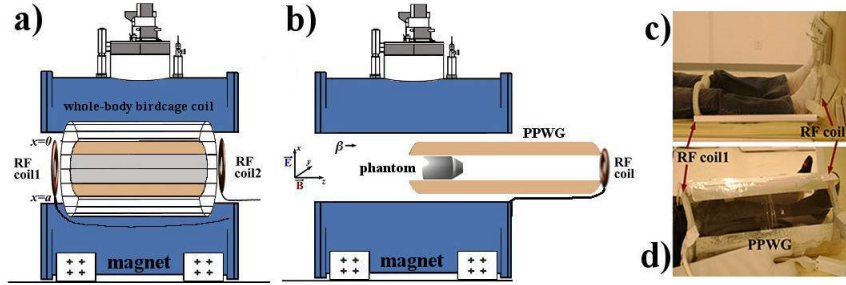


Figure 1. Experimental setups using the PPWG with aluminum plates for; a) simulation experiments using the PPWG inside the magnet bore filled with a cylindrical phantom and, b) determination of the *PSF* showing boundary conditions and the TEM mode propagation direction, β (Eq. 5) using a pair of RF surface coils: the distance between the phantom and the coil was 150 cm, c) Photo showing leg and RF coils positions for image acquisitions with pair of RF coils, and d) Photo of leg position and location inside the PPWG.

The plates were made out of aluminum sheets and 1 V was applied in all simulations. Both coils were tuned to 128 MHz and modeled using impedance boundary conditions according to the software-provider company. The excitation port was driven at the same resonance frequency. These computations also included simulated phantoms: a) cylindrical phantom ($\sigma = 1.5054 \text{ S/m}$ and $\epsilon_r = 69.062$), and b) a stylized simulation phantom of a male was developed using simple geometrical figures and based on the work by Fisher and Snyder [13] and Kerr et. al. [14]. Our phantom was divided into 3 important regions: 1) a sphere representing the head, 2) a box and a trapezoid representing the chest and abdomen respectively, and 3) 8 ellipsoids representing lower and upper extremities. These geometrical structures were joined together to create the whole-body phantom. This phantom was entirely designed with the COMSOL graphical tool. Fig. 4.a) shows a schematic of the phantom. FEM simulations of the SAR were also calculated for the same simulation setup.

4 Waveguide prototype

To test the viability of this traveling-wave approach at 3 T, two PPWG prototypes were built: a) aluminum foil (6 μm thickness) was laid on polycarbonate sheets separated by a 50 cm gap and the waveguide plates were 45 cm wide and 160 cm long, and b) an acrylic cylinder and two aluminum strips (25 cm wide and 60 cm long and 6 μm thickness): strips were equally spaced and mounted on the cylinder (30 cm diameter and 60 cm long). To avoid interference with the field gradients, plates of both prototypes have the same thickness. The the mechanical properties of the first prototype allows us to have constant cross-section for this particular length (Fig. 1.b)). It was used to test both the feasibility of travelling-wave approach and performance of the MR scanner. The second prototype was dedicated only to acquire images of a human leg. PPWG prototypes were used together with a whole-body birdcage (68 cm long, 66 cm diameter and 16 rungs and quadrature driven) for RF transmission, and reception was performed with a vendor-provider coil array (Philips Medical Systems, Best, NL) with two circular-shaped elements (11 cm diameter). Fig. 1.d) shows a photograph of the second waveguide prototype. The received-only circular coils were positioned at both ends of the cylinder. Fig. 1.a) shows an illustration of the waveguide and the experimental setup.

5 Methodology

All imaging experiments were carried out on a 3 T Philips imager (Philips Medical Systems, Best, NL) and operated under conventional mode for clinical practice. Standard gradient echo pulse sequences were also used in all cases. The first PPWG prototype as used for the optimal flip angle, B1 mapping and PSF experiments and according to the experimental setup shown in Fig. 1.b). The second prototype was used for the human leg imaging experiments only and the experimental setups of Fig. 1.a).

5.1 Optimum flip angle and B1 mapping

Gradient echo sequences are normally used for twMR imaging but no reference is given as to the optimal flip angle to be used [3-4]. To experimentally determine the optimal flip angle for transmission of the RF waves of the twMRI experiments with the PPWG, the image SNR was computed using phantom images acquired at different flip angles. T1-weighted images were acquired from 15° to 90° with a 15° step. Imaging experiments were conducted with the following parameters: TR/TE = 1500/7.6 ms, FOV = 240x240 mm, matrix size=288x224, slice thickness = 5 mm, NEX = 1.

Accurate spatial information can be obtained via the computation of B1 field mapping. As an attempt to solve the controversy of travelling-wave MRI at 3T, we performed B1 mapping. Imaging experiments were conducted using a PPWG, and 8-coil array for reception and a whole-body birdcage coil for transmission at 128 MHz. A spherical phantom was located at the magnet isocentre and the reception coil array was 100 cm away as in the previous experiment. Images were acquired with the parameters above. B1 maps were then calculated according to the method reported in [15] and, a reference T1-weighted image was also acquired using TR=350 ms, NEX=4 and the rest of the parameters above.

5.2 Imager performance

We used the point spread function (*PSF*) to measure performance of a 3T imager when used with a PPWG for travelling-wave MRI experiments. The *PSF* characterizes the response of an imaging system to a point source. This parameter is able to predict of how the object will be imaged, assuming a linear imaging process. The output image may then be regarded as a two-dimensional convolution of the ideal image with the *PSF*:

$$Image_{output} = Image_{ideal} \star PSF \quad (11)$$

T1-weighted images were acquired for the *PSF* experiments with the following acquisition parameters: Flip angle = 20° , TR/TE = 336.9/16.1 ms, FOV = 450 mm x 190 mm, matrix size = 500x169, slice thickness = 10 mm, NEX = 5. Images were Fourier transformed for the convolution in Eq. (11) and finally calculate the image *PSFs*. Two imaging experiments were performed to measure performance of a PPWG in twMRI experiments and for comparison purposes. Images were acquired with an 8-coil array operated in reception only, and transmission was carried out with the whole-body birdcage coil for: a) standard imaging experiments, and b) the PPWG and the surface coil. The first experiment was intended for comparison purposes.

5.3 Travelling-wave imaging experiments

All imaging experiments were conducted according to the Bioethical Committee of The Universidad Autonoma Metropolitana Iztapalapa. The healthy volunteer gave his permission and signed an informed consent form. The waveguide is long enough and its diameter wide enough to accommodate an entire human leg. The volunteer's leg (height=1.54 m, weight=54 Kg) was 75 cm long and located in the waveguide as shown in Fig. 1.d) to acquire images. T1-weighted images of an entire leg were acquired for three cases: a) the whole-body birdcage coil for transmission and reception, b) a pair of coil for reception together with the whole-body birdcage coil for transmission, and c) the PPWG and the pair of surface RF coils for reception and the whole-body birdcage coil for transmission. The birdcage coil was quadrature-driven, and the reception coils were linearly driven. The following acquisition parameters for the three experiments were used: flip angle = 80° , TR = 500 ms, TE = 4.6 ms, FOV = 484x171 mm, matrix size = 840x238, slice thickness = 5 mm, NEX = 10.

6 Results and Discussion

From Eq. (6), the cut-off frequency ($f_{cut-off} = 0$) for the principal mode of the PPWG allows the transmission of all the MR signals. This property of the PPWG offers the advantage to be used in MRI applications with larger fields-of-view for different magnet bores. The numerical computations of the magnetic fields of a PPWG using the TEM along the z -direction and different Larmor frequencies were computed using FEM, as shown in Fig. 2.

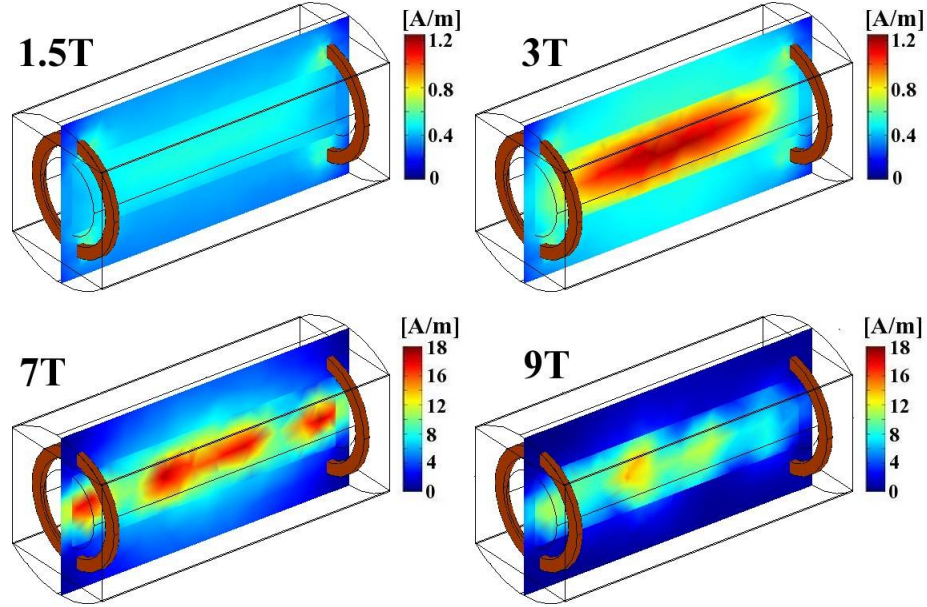


Figure 2. FEM numerical simulations of $B1+$ distributions for the setup in Fig. 1.a) at different magnetic field magnitudes. A substantial increment in the $B1+$ magnitude can be appreciated as the resonant frequency increases. However, the field pattern does not seem to be the same: the 1.5T simulations shows a pretty uniform behavior, contrary to the other simulations.

A clear concordance can be seen with those simulations reported by Brenner and co-workers [5]. An increment in the magnitude of $B1$ with the field strength can be observed. The numerically acquired magnetic fields at 7 T and 9 T show magnitudes in the same range. A very similar situation is obtained for the 1.5 T and 3 T cases. A

maximum theoretical 10-fold increase in the magnetic field strength was numerically obtained for the 7 T and 9 T simulations compared to those simulations at lower field intensities under the same conditions. Field-uniformity plots were computed using the simulation data of Fig. 2 and are shown in Fig. 3. All distribution magnetic field profiles were calculated along the gray line as indicated in Fig. 3.b). The B1 field distributions are reasonably smooth with a fairly analogous pattern, although for the 3 T case, a better field uniformity can be observed. The B1 field at 3 T shows a smoother uniformity and almost no attenuation along the length of the waveguide. Meanwhile, for the 1.5 T TE mode simulation, B1 constant distribution with a significant decrease can be observed. At high field, the 9 T simulation shows a reasonable variation in the B1 magnitude and does not suffer much attenuation along the propagation of the TE mode. These results are very encouraging because the waveguide was dielectrically loaded and represented by the cylindrical phantom and the resulting 3 T field uniformity is very good.

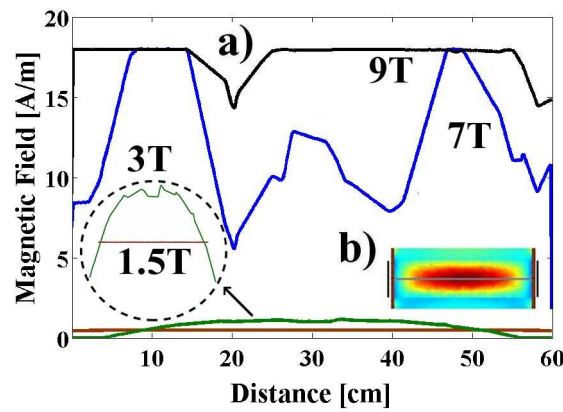


Figure 3 a) Comparison plot of B1+ field distributions along the waveguide for the field simulations of Fig. 2. The 1.5T B1+ magnitude is constant along the waveguide, while the other frequencies show a clear increment towards the centre. The 7T and 9T profiles tend to have a pretty similar magnetic field magnitude. b) All profiles were taken along the grey line.

The FEM-simulated B1 distribution of a simulated leg for the principal mode was also acquired and is shown in Fig. 4.b). Despite the fact that a simulated human leg representing a more complex condition was introduced in the simulations of B1 fields (Fig. 4.a)), by simple inspection the same pattern as that for the cylindrical phantom simulation is obtained for the magnetic field. From Figs. 3.a) and 4.a), an increment in the B1 field intensity at the very centre of the waveguide for both 3 T simulations can be observed. This is related to the frequency of the transmitted RF waves rather than the waveguide itself.

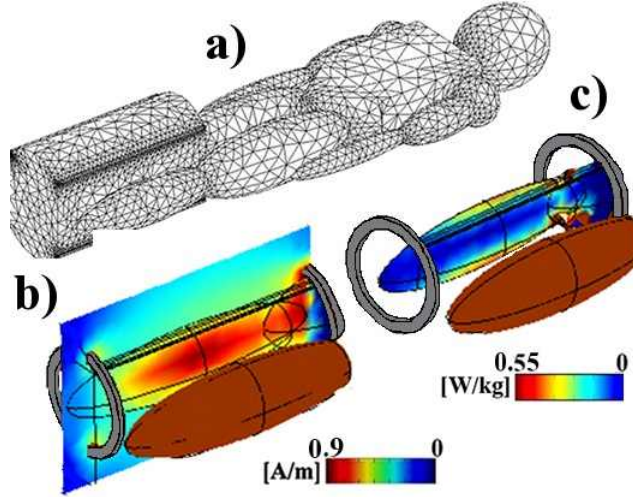


Figure 4. Simulated magnetic field distribution obtained at 3T for the TEM mode and SAR pattern of a phantom leg. The TEM simulation shows a higher magnitude at the centre of the leg, and the magnitude decreases towards the ends of the PPWG. A strong signal along the the periphery and weak signal otherwise. A similar pattern to the one in the phantom simulation (Fig. 2) was found for B1 simulations at 3T. SAR values are within accepted limits for humans.

Additionally, the distribution of the simulated B1 field for the simulated human leg was also determined and is shown in Fig. 5.a). A similar peak was produced by the waveguide and the leg at the waveguide centre, as in the previous numerically acquired calculations for the cylinder simulations.

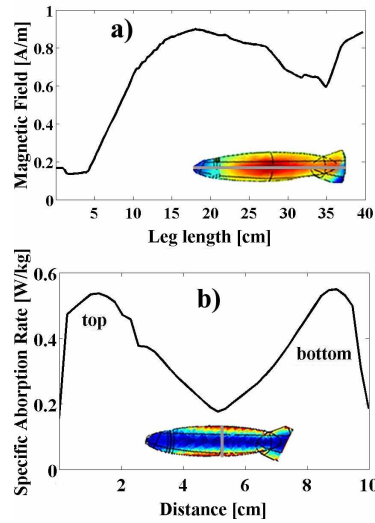


Figure 5. a) Distribution of magnetic field along the waveguide filled with the simulated leg of Fig. 4.b). b) SAR distribution computed from simulation data of Fig.c): the two peaks represent the hotspots in the simulated leg. Distributions were taken along the grey lines in the simulated leg for each case.

The FEM simulations were also used to verify the RF safety via the SAR and the simulation setup of Fig. 1.a) with the simulated human leg. Fig. 4.c) shows the SAR map of the simulated human leg. From this, SAR hotspots

are formed along the periphery and observed on the anterior and posterior faces of the simulated leg, where SAR reaches its maximum of 0.55 W/kg. An SAR distribution profile was also computed. Fig. 5.b) shows the graph of the SAR distribution taken from the simulation data of Fig. 4.c). However, although this numerical approach is limited, because only simple geometrical figures were used to build the human phantom, it still can be of some importance to understand the mechanisms involved in the formation of the magnetic fields generating the MR images with the PPWG for various Larmor frequencies.

T1-weighted images of a spherical phantom using the experimental arrangement of Fig. 1.b) were acquired for different flip angle values to determine the optimal flip angle for RF wave transmission. Figs. 6.a)-f) show the phantom images so from this image data, a plot of flip angle-vs.-SNR was calculated and shown in Fig. 6.g). From this plot, it can be appreciated that the maximum image SNR is reached at $\pi/2$. Therefore, a flip angle around this value should be adequate for these type of travelling-wave experiments.

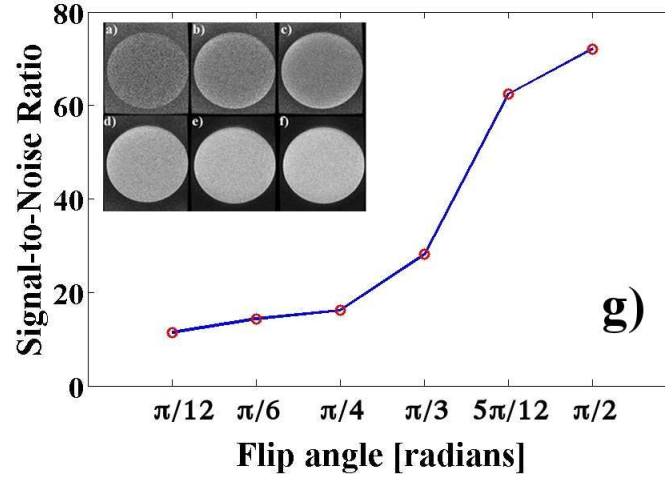


Figure 6. T1-weighted phantom images were computed for various flip angles (a)-f)) and a plot of flip angle-vs.-SNR (g) was computed using the experimental configuration of Fig. 1.b). An increment on the SNR can be observed as the flip angle increases until finds its maximum at $\pi/2$. These results corresponds very well with the standard gradient echo sequences.

Previous to compute the B1 mapping, an attempt to acquire images without the PPWG was performed and no signal was detected by the coil array. We think the RF waves have no mechanical conducting instrument to travel along to reach the distant object. A reference image was acquired with the coil array under standard conditions giving a SNR of 20.65, using an ROI of 70% of the total volume. Standard deviation was 5% below the mean signal intensity. The normalized B1 map and a profile of the field homogeneity were computed with the images acquired for the flip angle experiments. The reference and B1 map images are shown in Fig. 7.a) and b), respectively. the B1 map has a very good concordance with those reported in [3]. A homogeneity profile was also calculated with the Fig. 7.b) map and plotted in Fig. 7.c). The B1 map profile shows an excellent uniformity despite the fact that the images were acquired 1m away from the coil array and outside the imager.

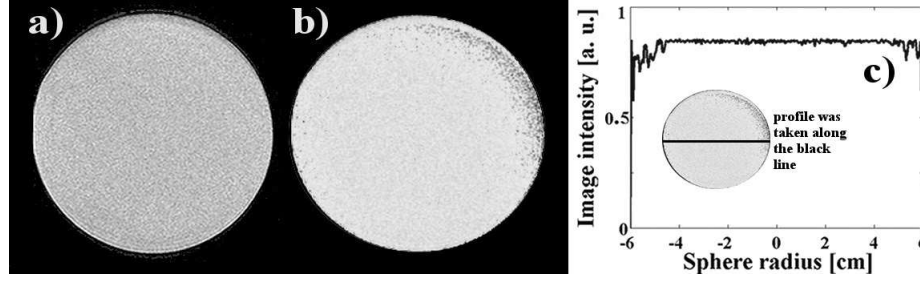


Figure 7. Reference T1-weighted image of a spherical phantom (a) acquired at 128 MHz and, the B1 map (b) and its corresponding uniformity profile (c) were computed. According to the uniformity profile in (c) the PPWG is able generate images with good quality. The RF waves were transmitted from the negative z-direction according to the experimental setup in Fig. 1.b).

This demonstrates that images generated with the PPWG have a good image quality compared to the standard image acquisition methods. It is important to highlight that the imager was operated using standard clinical protocols to acquire images and no modifications was done to the system.

Also, T1-weighted images were acquired for the evaluation of the imager performance using Fig. 1.b) configuration is shown Fig. 8.c). Fig. 8.b) shows an image obtained with the coil array and under standard conditions. With these images the corresponding *PSF* profiles were also measured together with Eq. (11) and shown in Fig. 8.a). The *PSF* profiles show a pattern as expected: the *PSF* of the PPWG shows a sharper and a slightly greater magnitude than the image acquired without the PPWG. From these profiles, we can infer that the PPWG did not cause any geometric distortion in the image and, that the system performance is not affected by the waveguide despite that the image was obtained far away from the coil array. Images were again obtained with standard imaging protocols and pulse sequences in a clinical imager. Uniformity profiles were also computed using Fig. 8.b) and c) images and shown in Fig. 8.d). Both profiles have a pretty similar behavior and magnitude. The SNR values of both experiments were: $\text{SNR}_{\text{PPWG}}/\text{SNR}_{\text{coil array}}=16.74/14.53$. This is a rather interesting result taking into account that the PPWG images were acquired 100 cm away from the coil array and outside the MR imager.

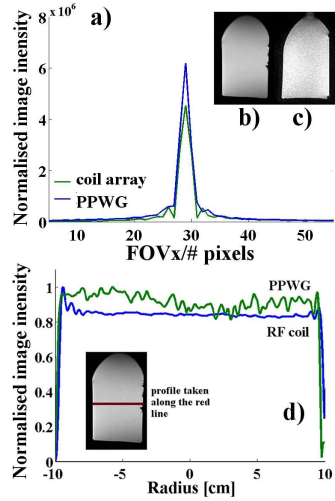


Figure 8. Profiles of the PSF for the coil array and PPWG+coil array (a) were computed from phantom images (b) and c)) to measure performance of the 3T imager. A moderately better performance is shown by the twMRI experiment. With these image data, uniformity profiles were also computed (d) showing a quite similar performance despite the fact that the coil array was 1 m away.

T1-weighted images of a healthy volunteer's entire leg were obtained using: a) the whole-body coil, b) the PPWG and c) a pair of RF coils are shown in Fig. 9. As shown, good quality images were acquired with this simple waveguide and the two circular-shape flexible coils. The FOV used to cover the entire leg is much larger than the coil size (11 cm diameter), and the B1 field is not attenuated along the entire leg; moreover at the waveguide ends, a signal increase is observed. An extra 5 cm can also be gained with the waveguide scheme. It is also important to highlight that one single FOV covering the entire leg was applied such that digital processing was not necessary as reported in [16]. Additionally, the leg image acquired with the pair of single RF coils (Fig. 9.c) shows really poor quality image. The regions near the two surface coils show very good contrast and a good image quality compared to the central region. Nevertheless, an increment in the noise level is also observed in the waveguide image (Fig. 9.b)) for the central region; this is likely due to the fold over effect caused by a FOV whose size is greater than the common FOV sizes used in clinical practice and, no fold over suppression was applied.

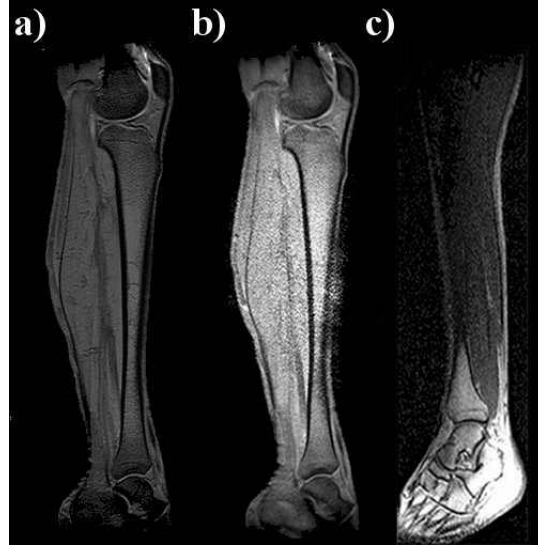


Figure 9. T1-weighted images of a human leg acquired with the whole-body birdcage coil (a) and PPWG + pair of RF coils (b) and the pair of coils only (c). The image acquired with the twMR approach shows an increment of noise at the centre of the leg not present in the other two leg images. The image obtained with the pair of coil shows a really poor signal compared to the other images. An evident signal contrast between the central and the foot regions can be appreciated: the higher image intensity can be explained by the close proximity of the coil to the foot (Fig. 1.c).

Another possible source of error is the image reconstruction scheme which is not the best suited for twMRI experiments. This is a matter of concern and deserves a thorough investigation. However, the performance of the travelling-wave approach shows a great potential for imaging large FOVs. The images in Fig. 9.a) and b) were normalized to the standard deviation of the image for comparison purposes and shown in Fig. 10. Comparison plots of image intensity distributions were also computed using the image data from Fig. 9 for both images. Fig. 9.c) image shows very poor image quality and it was not used in the image comparison.

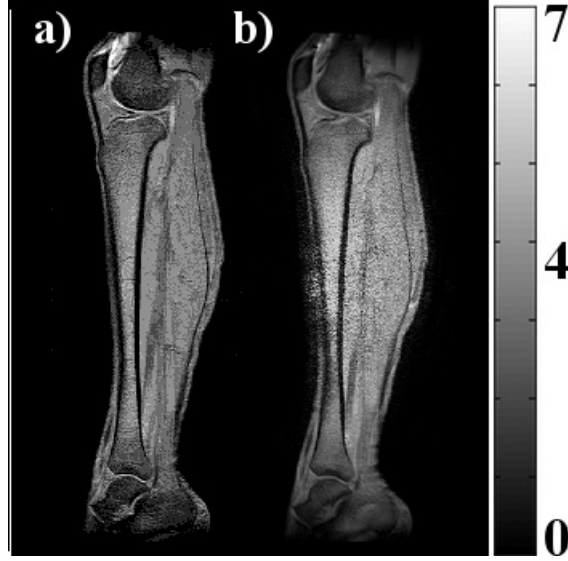


Figure 10. Comparison of normalized images acquired with the whole-body birdcage coil (a) and PPWG + pair of RF coils (b). Central region of (b) image is greater than the other leg image. Noise is probably due to the fold over effect and that no fold over suppression was applied.

Fig. 11 shows the distribution forms for both directions. The waveguide-acquired profile and the birdcage coil-acquired image show a pretty similar performance. The Fig. 4.b) simulation agrees very well with the experimental results shown in Fig. 11.b) for the PPWG-acquired image. In our study, the experimental and numerical results show that the restriction of a 7T/60 cm system is removed, allowing this approach to be used in a wider variety of applications involving imagers with much smaller magnet bores. The PPWG most likely has the simplest waveguide configuration available, allowing the travelling-wave approach to be implemented easily. It is much easier to build a waveguide like this and use standard surface RF coils to excite travelling-waves in a magnet bore. We suspect that by operating the coil array in the transceiver mode, the image SNR will be improved.

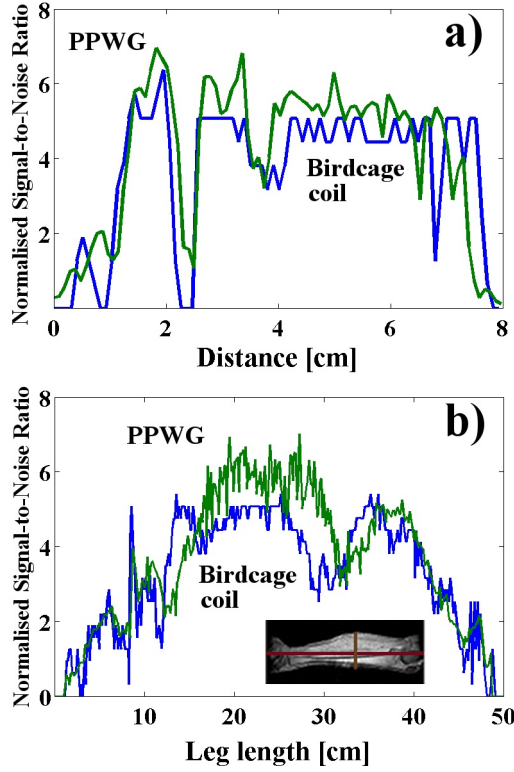


Figure 11. Comparison plots of normalized SNR distributions of Fig. 10 images, profiles were taken across the brown line (a) and along the red line (b) in the leg image. These profiles show a pretty similar pattern and performance. A strong concordance can be observed in (b) PPWG profiles with the B1 simulation profiles of Fig. 5.a).

7 Conclusion

We have experimentally demonstrated that the use of PPWGs can produce good SNR images for relatively large fields of view. We have shown that the waveguide approach can also be used with magnetic field intensities lower than 7 T and whole-body systems. Overcoming the limitation of a cutoff frequency, as demonstrated in this work, provides further freedom of implementation in a variety of geometries and for multinuclear operation, or for measuring several or extended samples along a waveguide. Further investigation is required to explain the physical mechanisms involved in the RF signal with a dielectric object inside a waveguide and its implications on image quality. A natural step ahead is to extend this approach to acquire images of the entire human body. These results pave the way to a further implementation of the travelling-wave approach in other applications using lower magnetic field intensities with bores of different dimensions.

Acknowledgments

We would like to acknowledge financial funding from CONACYT-Mexico under grant no. 166404 and Ph. D. scholarships.

References

- [1] Brunner DO, Zanche ND, Frohlich J, Paska J, Pruessmann KP. Travelling-wave nuclear magnetic resonance. *Nature*. 2009;457:994–999.
- [2] Brunner DO, Pruessmann KP. Reciprocity Relations in Travelling Wave MRI. *Proc. Intl. Soc. Mag. Reson. Med*. 2009;17:2943.
- [3] Mueller M, Alt S, Umathum R, Semmler W, Bock M. Targeted Traveling Wave MRI. *Proc. Intl. Soc. Mag. Reson. Med*. 2010;18:428.
- [4] Brunner DO, Paska J, Froehlich J, Pruessmann KP. Traveling-Wave RF Shimming Parallel MRI. *Mag. Reson. Med*. 2011;66:290-300.
- [5] Brenner D, Geschewski F, Felder J, Vahedipour K, Shah NJ. Experimental Verification of Numerical EM Field Simulations for Ultra-High Field Travelling Wave MRI. *Proc. Intl. Soc. Mag. Reson. Med*. 2011;19:1907.
- [6] Geschewski F, Felder J, Shah N. Optimum Coupling of Travelling Waves in a 9.4T Whole- Body Scanner. *Proc. Intl. Soc. Mag. Reson. Med*. 2010;18:1468.
- [7] F. Vazquez, R. Martin, O. Marrufo, A. O. Rodriguez, Waveguide Magnetic Resonance Imaging at 3 Tesla. *Proc. Intl. Soc. Mag. Reson. Med*. 2010;18:6484.
- [8] Cheng DK. *Field and Wave Electromagnetics*, 2nd Ed. Addison-Wesley, Reading, 1983. pp. 456-461.
- [9] De Flaviis F. Guided Waves, in *The Electrical Engineering Handbook*, W.-K. Chen, Elsevier Academic Press, Burlington, 2005, pp. 539-551.
- [10] Jin J. *The Finite Element Method in Electromagnetics*. New York: John Wiley & Sons, Inc., 2002.
- [11] Deibel JA, Escarra M, Berndsen N, Wang K, Mittleman DM. Finite-element method simulations of guided wave phenomena at teraHertz frequencies. *Proc. IEEE*. 2007;95:1624-1640.
- [12] RF Module Model Library, COMSOL: Burlington, 2008. p. 117.
- [13] Fisher HL, Snyder WS. Distribution of dose in the body from a source of gamma rays distributed uniformly in an organ. Report No. ORNL-4168, Oak Ridge National Laboratory, Oak Ridge, TN. 1967.
- [14] Kerr GD, Hwang JM, Jones RM. A mathematical model of a phantom developed for use in calculations of radiation dose to the body and major internal organs of a Japanese adult. Report No. ORNL/TM-5336, Oak Ridge National Laboratory, Oak Ridge, TN. 1976.
- [15] F. Vazquez, O. Marrufo, A. O. Rodriguez. Simple method for B1 mapping at 7 Tesla, *Proc. Eur. Soc. Mag. Reson. Med. Biol*. 2011;589:143.
- [16] Webb AG, Collins CM, Versluis MJ, Kan HE, Smith NB. MRI and localized proton spectroscopy in human leg muscle at 7 tesla using longitudinal traveling waves. *Magn. Reson. Med*. 2010;63:297–302.